


High-Energy Coherent X-Ray Diffraction Microscopy of Polycrystal Grains: Steps Toward a Multiscale Approach

S. Maddali^{1,*}, J.-S. Park,² H. Sharma,² S. Shastri,² P. Kenesei,² J. Almer², R. Harder,² M. J. Highland,² Y. Nashed³, and S. O. Hruszkewycz¹

¹Materials Science Division, Argonne National Laboratory, Lemont, Illinois 60439, USA

²X-ray Sciences Division, Argonne National Laboratory, Lemont, Illinois 60439, USA

³Mathematics and Computer Science Division, Argonne National Laboratory, Lemont, Illinois 60439, USA

 (Received 12 February 2020; revised 30 July 2020; accepted 31 July 2020; published 27 August 2020)

We present proof-of-concept imaging measurements of a polycrystalline material that integrate the elements of conventional high-energy x-ray diffraction microscopy with coherent diffraction-imaging techniques, and that can enable *in situ* strain-sensitive imaging of lattice structure in ensembles of deeply embedded crystals over five decades of length scale upon full realization. We demonstrate that the combination of these two characterization methods enables a more complete picture of the crystal-lattice strain than either method is capable of providing individually. Such complementary imaging capabilities are critical to addressing questions in a variety of research areas such as materials science and engineering, chemistry, and solid-state physics. Towards this eventual goal, the following key aspects are demonstrated: (1) high-energy Bragg coherent diffraction imaging (HE BCDI) of submicron-scale crystallites at 52 keV at current third-generation synchrotron light sources, (2) HE BCDI performed in conjunction with far-field high-energy diffraction microscopy (FF HEDM) on the grains of a polycrystalline sample in a smoothly integrated manner, and (3) the orientation information of an ensemble of grains obtained via FF HEDM used to perform complementary HE BCDI on multiple Bragg reflections of a single targeted grain. The imaged structures are seen to be 477 ± 50 nm or smaller in size, with an estimated strain resolution of 2.5×10^{-4} . These steps lay the foundation for integration of HE BCDI, which typically provides a spatial resolution tens of nanometers, into a broad suite of well-established HEDM methods, extending HEDM beyond the few-micrometer resolution bound and into the nanoscale, and positioning the approach to take full advantage of the orders-of-magnitude improvement of x-ray coherence expected at fourth-generation light sources presently being built and commissioned worldwide.

DOI: [10.1103/PhysRevApplied.14.024085](https://doi.org/10.1103/PhysRevApplied.14.024085)

I. INTRODUCTION

The ability to nondestructively measure local lattice distortion effects in crystalline materials with x-ray microscopy enables connections to be made between nano and microscale structures with macroscopic properties under working conditions, thus playing an important role in advancing materials science and engineering, chemistry, and solid-state physics. For example, recent successful studies include characterizing electrocatalytic processes *in situ* [1,2], informing the design of structural, functional, and quantum materials [3–5], and testing and validating theoretical models of polycrystals under various real-world stimuli [6,7]. Radiation of different energies in the hard x-ray regime is employed for a variety of such diffraction-based measurements at synchrotron light sources. At the lower end of this energy range (7–15 keV) where coherent

illumination is readily achieved, scattering methods such as Bragg coherent diffractive imaging (BCDI) and Bragg ptychography allow the measurement of the spatially varying lattice strain in single crystals with nanoscale resolution [3,8–11], and such approaches have recently been demonstrated for imaging individual grains in a polycrystal [12]. However, because the penetration length of these x-ray photons is typically a few tens of micrometers in dense solids, coherent diffraction-imaging methods cannot be used to interrogate grains deep within polycrystalline bulks beyond measurement of surface-facing grains [12–14]. At the other end of the hard x-ray energy range (higher than 50 keV), high-energy diffraction microscopy (HEDM) techniques that do not rely on beam coherence permit the imaging and volume-averaged strain characterization of thousands of grains in a polycrystalline bulk of up to a millimeter in size [15,16]. Querying such large samples in this manner becomes possible owing to the enhanced penetration at high x-ray energies, and the current state of the

*smaddali@anl.gov

art in HEDM allows the average strain state, lattice orientation, unit-cell structure, and morphology of individual grains that make up the polycrystal to be determined at a spatial resolution of about $1.5 \mu\text{m}$ [16].

Presently HEDM and BCDI have their respective places in materials research, with each permitting the measurement of complementary portions of the crystal-lattice strain (in general, a spatially varying quantity, see Appendix D for details). Combining the two techniques into a single multicomponent microscopy approach presents a tremendous opportunity to characterize lattice strain in multiple polygrains in a manner not yet achieved. A composite measurement scheme that draws from the strengths of both methods could potentially open the door to a wide range of possibilities in materials characterization by enabling strain imaging of bulk materials with highly intricate crystallographies and domain morphologies, resolved from millimeters to nanometers. Measurements of this kind enhance our understanding of grain and interface dynamics in solids by enabling access to length scales that elucidate a variety of lattice distortion features (such as macroscopic stress concentration sites down to individual dislocations), and present immensely valuable insights. One important example is that of the mechanical behavior of bulk polycrystalline structural materials, for which fully descriptive models of deformation and failure have not been fully realized despite decades of study [17]. Further progress towards this and other important materials questions depends on *in situ* experimental methods that can measure structural processes over many length scales, as could be realized by combining the HEDM and BCDI modalities.

Several critical steps towards the unification of BCDI and HEDM are demonstrated in this paper, anticipating the capabilities of fourth-generation light sources coming online worldwide now and in the near future [18]. These upcoming synchrotron light sources provide a several-hundred-fold increase in coherent x-ray flux as compared to today's facilities, making high-energy BCDI practical and routine. In this context, a high-throughput materials characterization capability that makes use of high x-ray energies and that consists of combined and fully integrated HEDM and BCDI modalities is realizable. We present proofs of concept of several elements of such a measurement using x rays with an energy of 52 keV at the Advanced Photon Source, a third-generation 7-GeV synchrotron equipped with a superconducting undulator for enhanced photon flux [19]. Several key aspects are established:

1. With the appropriate adaptation of HEDM x-ray optics, it is possible to implement HE BCDI on an isolated submicron-scale crystal at 52 keV, provided partial coherence effects of the x-ray beam are accounted for.

We provide corroborative calculations for estimating the coherence lengths.

2. It is possible to integrate far-field HEDM (FF HEDM) and HE BCDI and to make these measurements in succession on individual grains in a polycrystalline material.

3. In a polycrystal, the orientation information of each grain within a broad illumination footprint that is obtained from FF HEDM can be used to efficiently perform HE BCDI on multiple Bragg reflections of a single grain within a wide window of reciprocal space, a capability that is extremely difficult to realize in a standalone BCDI measurement.

These demonstrations, detailed below, lay the foundation for a flexible multimodal means of studying polycrystalline materials in situations where the long penetration depths of high-energy x rays is critical.

II. DEMONSTRATION OF HE BCDI

The ability to perform HE BCDI measurements with nominally partially coherent illumination is a key requirement for the eventual integration of the HEDM and BCDI measurement modalities. For our study, it is important to demonstrate this type of unconventional measurement at a third-generation synchrotron facility presently used for conventional HEDM measurements. Such a facility (e.g., the 1-ID-E end station at the Advanced Photon Source) is not optimized for coherent diffraction measurements at high energies, both in terms of the available x-ray optics and the diffractometer setup. The success of an HE BCDI measurement at such a facility with the available x-ray source and infrastructure, and the subsequent imaging establishes beyond doubt the ability to perform the most crucial part of a multiscale characterization experiment, i.e., spatial resolution of polycrystal-lattice strain. This prospect is particularly significant at future high-energy, high-coherence facilities, such as ESRF-EBS and the soon-to-be-upgraded Advanced Photon Source. To this end, one of the goals of our study is to ascertain the optimal configuration suitable for HE BCDI at the presently available high-energy beamline, by imaging a nominally strain-free and well-faceted crystal (namely, a gold particle obtained by dewetting a gold film on a silicon substrate, hereafter referred to as a “submicroparticle”). A simplified schematic of the x-ray optical configuration settled upon for this purpose is shown in Fig. 1(a), which yielded a suitable coherence volume and detector geometry at 1-ID-E (see Appendix A). The critical components needed to realize this are white-beam slits opened to $0.5 \times 0.5 \text{ mm}^2$, a collimating lens, a high-resolution monochromator ($\Delta E/E \sim 10^{-4}$ at $E = 52 \text{ keV}$) [20], a vertically focusing sawtooth lens [21], a sample-detector distance of

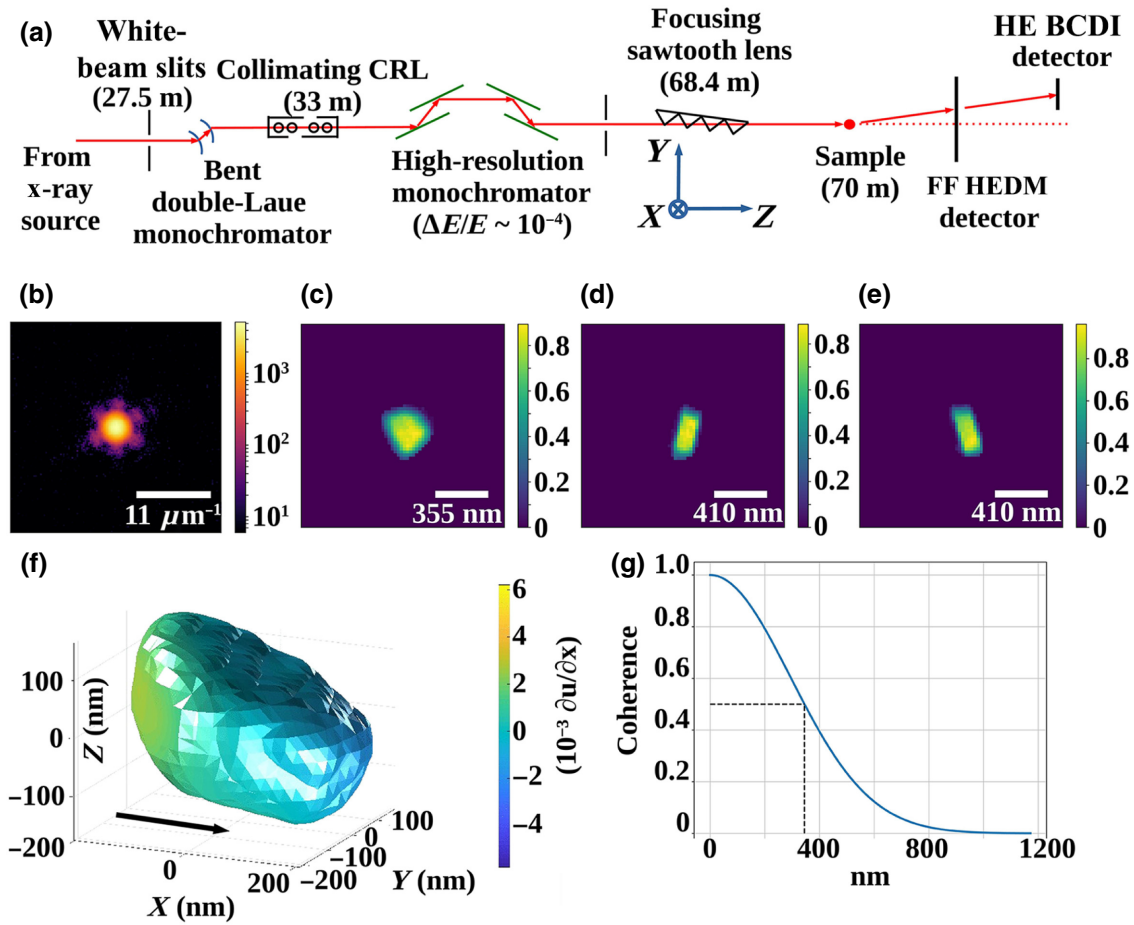


FIG. 1. (a) Simplified schematic of Beamline 1-ID-E at the Advanced Photon Source, showing the essential components in the laboratory frame of reference. The X axis goes into the plane of the figure. Only the top sawtooth lens is used to provide focus. See Appendix A for details on why this configuration is chosen. (b) Central slice of the partially coherent three-dimensional (3D) diffraction signal from the gold submicroparticle. Color scale denotes photon count. (c)–(e) Amplitude cross sections of the gold submicroparticle after phase retrieval. Color scale denotes the amplitude of the reconstructed complex-valued object in arbitrary units. See Appendix E for the spatial resolution of this measurement. (f) Lattice strain profile on the surface of the 3D submicroparticle. The arrow indicates the positive X direction in the laboratory frame. (g) Profile of the Gaussian coherence function along the direction of the arrow shown in (f). The half-width at half-maximum is an estimate of the X -transverse coherence length of the beam.

6.12 m, and a finely pixelated photon-counting area detector with good quantum efficiency at 52 keV (Lynx 1800 detector manufactured by Amsterdam Scientific Instruments (ASI), with a Medipix3 chip and a $55\text{-}\mu\text{m}$ pixel pitch). With this arrangement, a $1.5 \times 50\ \mu\text{m}$ beam is delivered to the sample. The detector is mounted along the far wall of the experimental enclosure with the 2 degrees of freedom (radial distance R and azimuthal angle η) capable of capturing higher-order Bragg reflections within a scattering angle approximately 15° .

With this arrangement, the three-dimensional diffraction pattern in the vicinity of a $[111]$ Bragg peak from the gold submicroparticle is measured using the high-precision sample manipulation system at the 1-ID-E end station [22]. The sample is oriented such that the x-ray beam passed through the silicon substrate exactly once en route to the

detector. The rotation angle ω of the sample is incremented about the vertical axis in fine steps of $\Delta\omega = 0.01^\circ$ spanning a total of 0.6° about the angle of the Bragg peak maximum. At each sample angle, area detector images of the diffraction patterns are collected with an exposure time of 600 s per angle. The three-dimensional intensity data acquired in this manner encoded the morphology and the lattice distortions of the diffracting crystal.

The complete measurement of the gold submicroparticle consisted of 25 HE BCDI scans over the same angular interval. Between successive scans, any possible drift of the submicroparticle is corrected for by readjusting the position of the sample within the beam. The rotational stability of the submicroparticle during the entire scan period is monitored through the “rocking curve,” i.e., the aggregate detector intensity as a function of the angular

position of the scatterer. This plot, shown for successive scans in Fig. 9 of the appendix, indicates no appreciable change in the orientation of the submicroparticle during the scan. A two-dimensional (2D) slice of the diffraction around the Bragg peak is seen in Fig. 1(b), in which the fringes are oversampled (as typically required in BCDI [23]), but showing that the fringe contrast is less than 100%, indicating partially coherent illumination. The 3D image of the scatterer is reconstructed using a BCDI phase-retrieval approach that accounts for partial coherence, based on recently published methods [24–26]. Within the phase-retrieval algorithms used, the partial coherence correction is achieved by modeling the measured diffraction as a convolution of the fully coherent diffraction intensity pattern with a blurring kernel [24–26], which is chosen to be a multivariate Gaussian. The phase-retrieval recipe consisted of alternating cycles of the Gerchberg-Saxton error reduction and hybrid input-output [27] along with intermittent updating of the real-space support via a shrinkwrap algorithm [28] and optimization of the six parameters of the unknown Gaussian blurring kernel (see Appendix B for the exact phase-retrieval algorithm and kernel parameterization). Prior to phase retrieval, the measured diffraction pattern is shifted in its numerical array so that the high-intensity center coincided with the center of the array. This guaranteed the removal of phase ramps in the final reconstructed object. Importantly, this step also ensured that any spatially homogeneous strain (which also manifests as a phase ramp in the recovered complex-valued scatterer) is removed. As we demonstrate in Sec. V and Appendix D, this “volume-averaged” strain component is in fact measured by FF HEDM for the polycrystal grains even though it is ignored in the HE BCDI measurement.

This approach results in a complex-valued real-space image of the diffracting crystal ρ that encodes information about lattice displacement distribution within the particle. Specifically, the phase of ρ is related to the projection of the spatial distribution of atomic lattice displacement perturbations \mathbf{u} along a reciprocal lattice vector \mathbf{Q} [10], such that $\rho = |\rho| \exp(2\pi i \mathbf{u} \cdot \mathbf{Q})$. Via the phase of ρ (i.e., $\angle \rho$), one can obtain a component of the displacement field: $u_{111} = \angle \rho / |2\pi \mathbf{Q}_{111}|$. Subsequently, the component of the strain tensor along \mathbf{Q}_{111} can be determined at a location x_{111} , by computing the partial derivative $\partial u_{111} / \partial x_{111}$.

Figures 1(c)–1(e) show the amplitude cross sections of the reconstructed submicroparticle (i.e., $|\rho|$), obtained from phase retrieval. The spatial resolution of this measurement is estimated to be around 52 nm, obtained by fitting an error function to the rising edge of the amplitude cross sections shown in these figures (see Appendix E for additional details). Figure 1(f) shows a 3D image of the particle with the color scale representing the surface variations of the strain component $\partial u_{111} / \partial x_{111}$. The particle itself has a maximum diameter of about 400 nm,

displays distinct facets, and has relatively low levels of strain—all characteristics of gold particles obtained by dewetting [29].

The arrow in Fig. 1(f) indicates the horizontal (X) direction in the laboratory frame, and the profile of the real-space representation of the blurring kernel along this direction is shown in Fig. 1(g). We find that in this direction the half-width at half-maximum of the Gaussian kernel is about 350 nm. This length is a rough estimate of the 50% coherence threshold in that dimension.

This result establishes a baseline for the HE BCDI methodology and suggests that with the x-ray optical setup employed in this work, crystallites with diameters corresponding roughly to the 50%-coherence threshold of the beam can be imaged with HE BCDI. Crucially, this HE BCDI reconstruction of a symmetrically faceted, relatively strain-free submicroparticle provided a sufficiently well-constrained measurement of the blurring kernel that can be used to model the partial coherence of the x-ray beam for subsequent HE BCDI measurements of individual grains that, in general, display more disordered fringe patterns owing to potentially greater extents of lattice strain and less regular faceting.

III. INTEGRATED FF HEDM AND HE BCDI MEASUREMENTS

To demonstrate the integration of the HE BCDI measurement modality described above with standard HEDM measurements, we utilize a polycrystalline gold film [12], which is deposited by electron-beam evaporation on an amorphous carbon substrate. The film thickness is around 300 nm, with a characteristic in-plane grain size of 400 nm. A schematic showing the different detectors used in the combined FF HEDM and HE BCDI experiment is shown in Fig. 2. The sample is oriented with the substrate surface initially normal to the incident beam, and first measured with FF HEDM. The line-focused x-ray beam obtained with the vertical sawtooth focusing lens has a footprint on the sample of $1.5 \times 100 \mu\text{m}^2$, with an x-ray energy of 52 keV, as before. The FF HEDM measurement is performed by rotating the sample about the Y axis through 360° using a high-precision Aerotech rotation stage (designated ω in Fig. 2) that scanned the sample in angular increments of 0.01° , resulting in 36 000 acquired diffraction images. Bragg peaks are measured during this scan with a bank of four GE-41RT detectors positioned approximately 1 m from the sample with $200\text{-}\mu\text{m}$ pixels that subtended complete Debye-Scherrer rings out to scattering angles of up to approximately 15° . Over the course of the entire scan, tens of thousands of diffraction peaks are collected, corresponding to the $\langle 111 \rangle$, $\langle 200 \rangle$, $\langle 220 \rangle$, and $\langle 311 \rangle$ Bragg reflections of the fcc gold lattice. A visualization of a subset of these measured Bragg peaks is shown in Fig. 3, in which the distinct Debye spheres of each order of

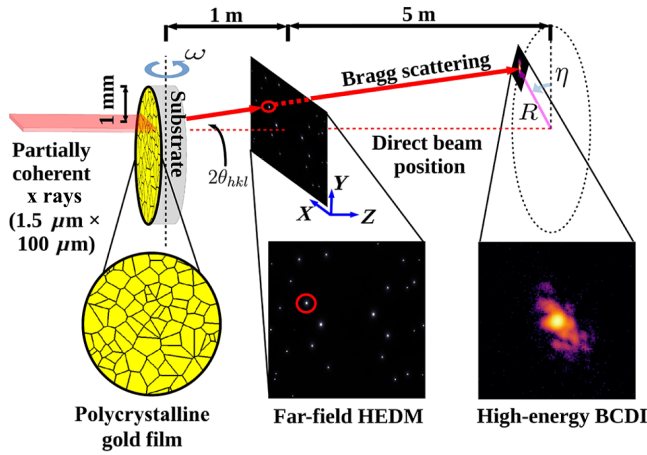


FIG. 2. Schematic of the multiscale measurement technique with the HEDM and BCDI components. The FF HEDM measurement is made at a scattering distance of 1 m while the HE BCDI measurement is made at a scattering distance of 6 m. The detector images, respectively, denote the relatively coarse resolution of the Bragg peaks from the grains in the sample (FF HEDM), and the finer details of the fringe pattern in the vicinity of one such peak. We note that the beam dimensions shown here only correspond to the FF HEDM measurement. The beam size is actually set to $1.5 \times 50 \mu\text{m}^2$ for all HE BCDI measurements.

Bragg diffraction from the illuminated grains are denoted by differently colored markers.

The analysis of the FF HEDM data reveals a total of 315 782 discernable Bragg reflections that survive the thresholding and background reduction process typically applied to the raw detector images. Subsequent peak indexing and grain mapping establishes that these reflections come from a total of 6768 grains. The Bragg peaks that are eventually chosen for HE BCDI had high orientation confidence, BCDI signal quality, and absence of stray scattering on the photon-counting detector. We estimate the number of grains actually illuminated by the beam during the entire 360° rotation of the sample is around 1667 assuming a beam-illumination footprint on the film of $1.5 \times 100 \mu\text{m}^2$ (i.e., the FF HEDM beam dimensions) when the film is placed perpendicular to the incident beam, and an approximate grain cross-section area of $300 \times 300 \text{ nm}^2$ (the dimensions of the reconstructed grain). The majority of the reflections captured on the detector evidently come from the remaining $6768 - 1667 = 5101$ grains, which periodically enter and exit the beam over the 360° sample rotation.

The HEDM software suite MIDAS [30,31] is used to automatically identify and index all of the peaks in the measured detector images and to map each peak back to one of the 6768 grains within the illuminated beam volume (with varying amounts of confidence). The details of this indexing process are given in Ref. [16], and is the

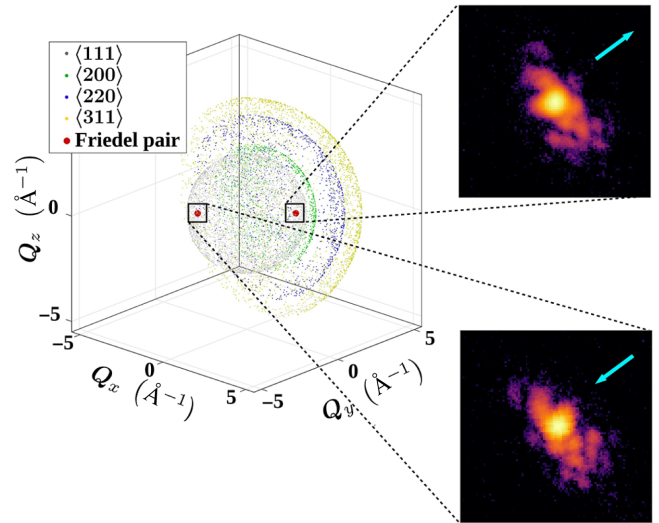


FIG. 3. Scatter plot of the reciprocal lattice points corresponding to the Bragg peaks from the illuminated grains, acquired during the FF HEDM measurement. Shown here is a subset of the observed Bragg reflections, up to the (311) reflection for fcc crystals. The bold markers denote a Friedel pair of (111) reflections from a single grain. Also shown are the enlarged central slices of the measured partially coherent diffraction signal in the vicinity of these reflections (reoriented to emphasize the centrosymmetry about the line denoted by the two arrows, corresponding to reciprocal lattice vector directions $\pm\mathbf{Q}_{111}$, respectively).

standard procedure for FF HEDM experiments. The quantities ω and η are determined up to an uncertainty of 0.01° . This provides angular information of sufficient precision in order to orient the sample and the ASI detector at 6.12 m from the sample for a HE BCDI measurement from a chosen grain in the polycrystal (described in the next section).

We note that both FF HEDM and HE BCDI measurements are made sequentially with the same arrangement of x-ray optics and goniometer hardware, differing only in the sample-detector distance and the detector module used. This demonstration points towards the potential of smooth physical integration of FF HEDM and HE BCDI, and also indicates the possibility of future integration with other high-energy microscopy imaging modes, including near-field HEDM (NF HEDM) [15] and diffraction-contrast tomography (DCT) [32]. Physically realizing this unification requires significant development that is currently ongoing, both in terms of improving the spatial resolution of near-field HEDM detectors and line focusing x-ray optics to reach submicrometer length scales (thereby overlapping with the demonstrated length regime of HE BCDI), and in terms of improving synchrotron storage ring technology that will enable HE BCDI of ten-micron-scale grains (thus intersecting with current NF HEDM capabilities).

IV. HE BCDI OF A BRAGG-PEAK FRIEDEL PAIR FROM A SINGLE GRAIN

The grain orientation and Bragg-peak indexing information from the FF HEDM measurement is used to measure and image two different Bragg peaks of the $\langle 111 \rangle$ family from the same grain with HE BCDI. Specifically, we seek to demonstrate unambiguously that the selected peaks indeed originated from the same grain by reconstructing HE BCDI data from a Friedel pair of Bragg peaks ($[111]$ and $[\bar{1}\bar{1}\bar{1}]$), which are centrosymmetric in the crystal frame, but not in the frame of the detector when in the Bragg condition (since going from one Bragg condition to the other involves a sample rotation about Y and a reorientation of the detector). Since Friedel pairs encode equivalent structural information due to their centrosymmetry (see Appendix C), the subsequent HE BCDI reconstructions are expected to show equivalent strain profiles. The absolute reciprocal space positions of the chosen Friedel-pair reflections (obtained via FF HEDM) are shown in Fig. 3, along with 2D images of the fringe detail about each of these peaks, obtained with the HE BCDI detector. The Friedel pair of peaks are located in centrosymmetric positions about the reciprocal space origin $\mathbf{Q} = 0$, and the enlarged view of these peaks provided by the HE BCDI detector images also shows consistent centrosymmetric fringe patterns.

This pair of peaks is chosen for validation of the multiscale measurement by the recovery of the (nominally) same strain field through unrelated, noncentrosymmetric diffraction geometries. Further, the diffracted signal is relatively strong from the originating grain, and the volume of reciprocal space in the vicinity of the peaks did not overlap with reflections from other grains. The HE BCDI measurements are similar to the case of the isolated gold submicroparticle (60 angular steps of size $\Delta\omega = 0.01^\circ$, each with an exposure of 600 s). Image reconstruction is done using the same phase-retrieval approach as above, accounting for partial coherence by utilizing the Gaussian blurring kernel determined from the isolated crystal as a starting guess and allowing further minor refinement of the Gaussian parameters during phase retrieval. The 3D image reconstructions from both centrosymmetric Bragg peaks are shown in Fig. 4 with surface-strain coloration. Also shown are cuts through the interior of the grain that show the spatial distribution of the strain component $\partial u_{111}/\partial x_{111}$. We see that the center of the grain is relatively strain free, while the regions of relatively significant strain are seen to be along the interfaces with neighboring grains (i.e., the grain boundaries).

In comparing the 3D image reconstructions, we immediately recognize that the two images are of the same grain, indicating that the two Bragg peaks that are measured from among tens of thousands emanating from the illuminated sample are indeed a Friedel pair. The morphology,

orientation, and strain state of the two images are very similar, as expected, and small differences can be ascribed to factors such as the low signal-to-noise ratios in these measurements and to the inherently different sampling of 3D reciprocal space in the two measurements. Importantly, the HE BCDI reconstruction gives access to the lattice distortion in the interior of this grain with a spatial resolution of 48 nm (see Appendix E), pointing to the broader potential of extending the HEDM technique (whose spatial resolution is about $1.5 \mu\text{m}$) with coherent diffraction imaging.

We now estimate the strain resolution of the BCDI reconstructions. We do this by calculating the spread in the strain distribution within the nominally constant-strain volume of the scatterers, as computed from the reconstructed phases. Figure 5 shows the distributions of this quantity for the central volume of the three BCDI reconstructions (submicroparticle, and $[111]$ as well as $[\bar{1}\bar{1}\bar{1}]$ reconstructions of the grain). The voxels sampled for these histograms are far away from the interfaces of the scatterers, where it is expected that the strain would be large due to the interface effects. The strain resolution is estimated to be 2.5×10^{-4} from the half-widths of the histograms.

We demonstrate that the same strain profile is obtained unambiguously from the diffraction data of both Friedel-pair twins, which are acquired from completely different, unrelated diffraction geometries and detector orientations. These two configurations in fact did not obey the centrosymmetry of the Friedel-pair directions in the laboratory frame. We see this as evidence that the observed strain field is in fact realistic. The physical origins of the observed strain profile depicted in Fig. 4 lie in the specific morphology of the grain of interest as well as the crystallographic misorientation with each of its neighbors. These factors conspire to impose highly nontrivial interface effects on the crystal lattice of the confined grain, particularly near the grain boundaries. The observed *scalar* field is but one component of a potentially highly intricate tensor strain field over the crystal lattice of the grain, facilitated by these influences.

This measurement demonstrates the efficacy of using information obtained from FF HEDM to efficiently execute a complementary HE BCDI measurement that resolves intra-granular strain fields critical to the behavior and properties of polycrystalline materials. Our work describes a demonstration involving two equivalent HE BCDI images of a single grain obtained from centrosymmetric Bragg peaks. However, the full power of the approach will be apparent at the significantly larger high-energy coherent flux levels at future fourth-generation synchrotron light sources. We will have the ability to swiftly measure many more nonequivalent Bragg peaks from a given polycrystal grain in order to spatially resolve the full six-component strain tensor, as has been painstakingly demonstrated for isolated nanocrystals at lower energies ($< 10 \text{ keV}$) [33,34].

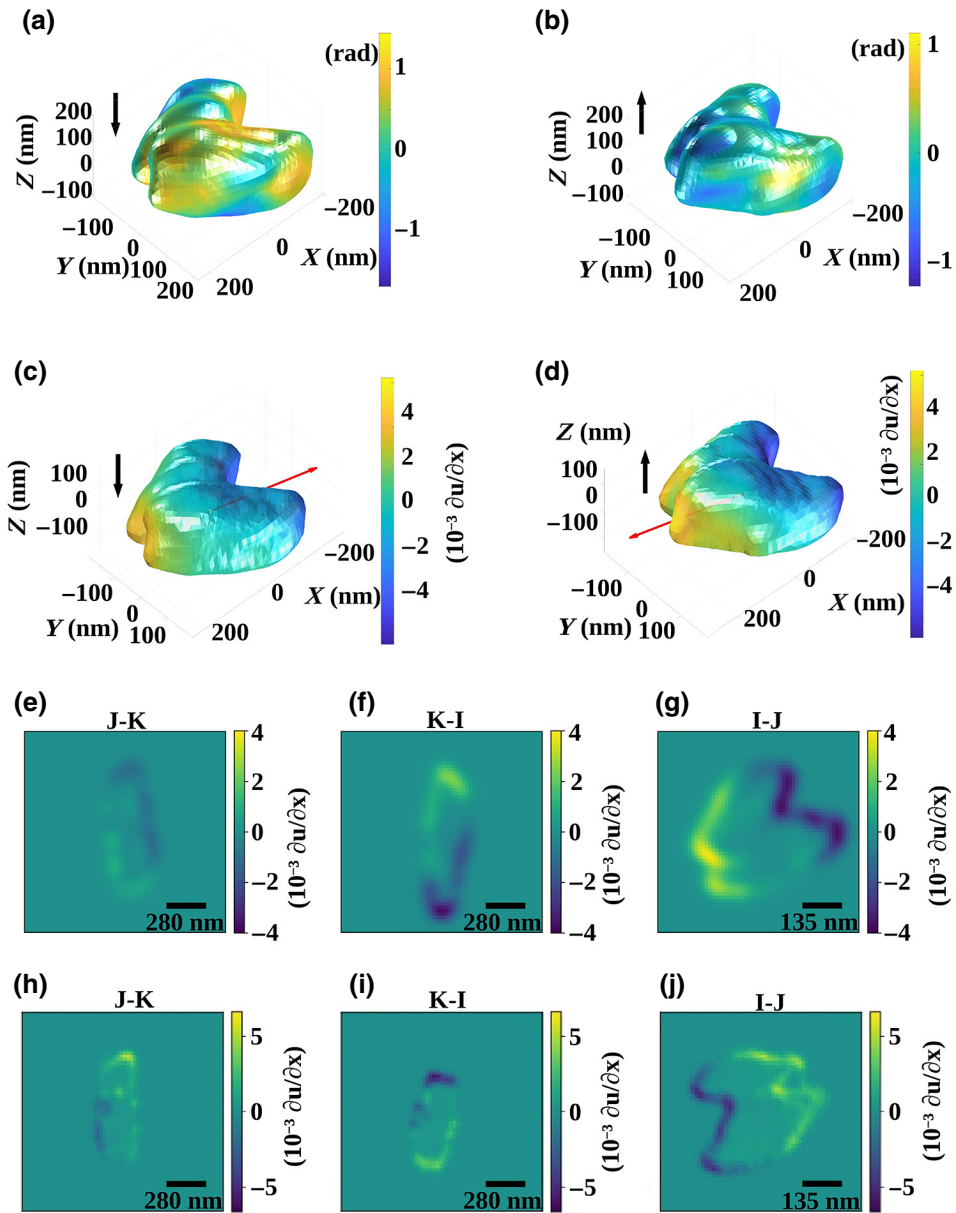


FIG. 4. (a) Reconstructed isosurface image of the grain of interest from the polycrystalline film (isovalue 20% of the maximum amplitude of the reconstructed object), obtained from the HE BCDI data set corresponding to the $[111]$ reflection. The phase field as determined by phase retrieval, is superposed on the grain surface. The raw phase is smoothed twice with a Gaussian kernel of size $1 \times 1 \times 1$ pixels in order to reduce the effects of pixelation prior to differentiation. This minimizes the effect of kernel-induced spreading while preserving the salient features. We provide images of the raw, unprocessed phase in Fig. 10 of the appendix, in which the pixelation artifacts are clearly visible. We see that the spatially resolved phase in one image is correspondingly inverted in the other image. The black arrow depicts the direction of the incident x-ray beam in the Bragg condition. (b) The same grain imaged from the data set corresponding to the $[\bar{1}\bar{1}\bar{1}]$ reflection. (c),(d) The corresponding lattice strain-field components, computed after kernel smoothing the phase field. The red arrow denotes the reciprocal lattice vectors $\mathbf{Q} = [111]$ and $\mathbf{Q} = [\bar{1}\bar{1}\bar{1}]$, respectively. All isosurface axis dimensions are in nanometers. (e)–(g) Strain-profile cross section of the grain reconstruction shown in (a), through the center of the grain. These images represent three mutually perpendicular slices of size 60×60 pixels in the numeric array (IJ, JK, KI). (h)–(j) Corresponding strain profile obtained from the reconstruction in (b).

In this regard, utilizing high-energy x rays is particularly appealing because it presents convenient access to higher-order Bragg peaks (as shown in Fig. 3), which provide

higher strain resolution and which are difficult or impossible to access at lower beam energies. As a step in this direction, we present an image reconstruction of another grain

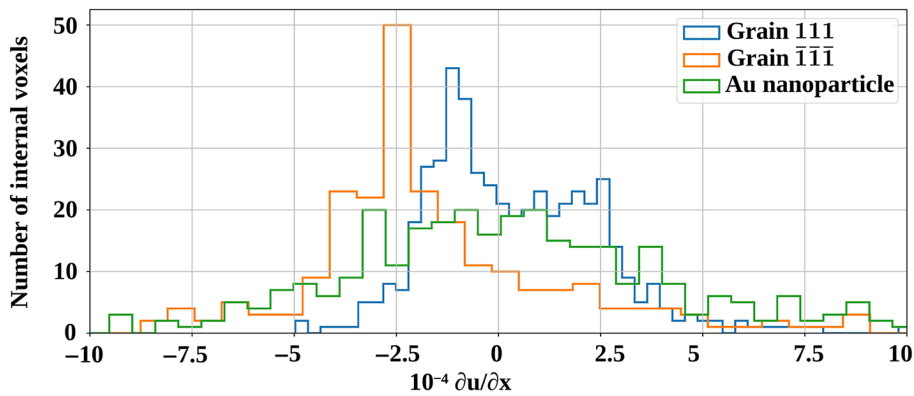


FIG. 5. Distributions of the strain component of the three BCDI reconstructions, taking into account only the internal voxels (far away from the grain boundaries) where strain is nominally zero. For all three reconstructions, the half-widths of the strain distributions are around 2.5×10^{-4} , which gives the estimated strain resolution of the nominally well-ordered lattices.

in the polycrystal film, obtained from a HE BCDI measurement from a (200) Bragg peak (see Appendix F), that represents another benchmark in the eventual realization of integrated multiscale measurements with high-energy coherent x rays.

V. DISCUSSION

A. Influence of refractive index

We briefly consider the influence of the refractive index (RI) of the diffracting material with respect to vacuum and the surrounding medium. In general, a BCDI diffraction pattern is influenced by the local lattice strain (a tensor quantity) as well as the locally varying phase as a result of material RI not equal to 1 (in general, a complex-valued scalar to account for material absorption). If the RI is significantly far from unity, the true optical path of the x-ray beam through the diffracting object is significantly more difficult to characterize owing to its specific morphology and size. Further complications may be introduced in the case of an embedded scatterer, where optical path lengths may be magnified depending on the distance traveled by the beam through the material prior to capture on the detector. In our case, we ignore this effect owing to the fact that the RI of gold (the material of the polycrystalline film) at a beam energy of 52 keV is known to be negligibly different from 1 (by about 10^{-6}).

B. Why high-energy x rays?

We point out another crucial role played by high-energy x rays in the multiscale measurement in addition to the deep penetration of bulk polycrystals. It facilitates the capture of higher-order Bragg reflections from the polycrystal during the preliminary FF HEDM measurement. This would be prohibitively difficult at lower beam energies owing to the significantly larger scattering angles (approximately 5 times larger from a beam energy ratio of 52 to 10 keV). The ability of the FF HEDM analysis software MIDAS [30,31] to assign an originating grain to an observed Bragg peak is predicated upon the collection of a sufficient number of reflections from that grain, used

internally to compute a “confidence” metric of the grain orientation. The higher this quantity (which ranges from 0 to 1), the more certainty with which the MIDAS software is able to map a reflection to its parent grain. The higher beam energy, therefore, facilitates a higher confidence in the grain orientation by allowing more orders of Bragg reflections to be successfully captured on the detector. It is with the use of high x-ray energies that specific Bragg reflections of a single grain in a vast polycrystal field may be located with certainty in this manner, in service of the subsequent HE BCDI measurements on individual reflections. Further, the error in the computed volume-averaged strain is smaller with the inclusion of higher-order Bragg reflections [see Eq. (C3) in the appendix, for the dependence of the strain component \mathcal{E} on the reciprocal lattice vector \mathbf{Q}].

C. HE BCDI and partial coherence

At the present time, Beamline 1-ID of the Advanced Photon Source is not optimized for coherent flux at beam energies greater than 50 keV, in order to perform a BCDI measurement. Under these circumstances, the configuration of the optical elements is improvised to allow for optimal coherent illumination of the scatterers. Without a sample-independent quantification of the beam coherence for this *ad hoc* arrangement, it is important to obtain alternative estimates of the coherence lengths and therefore establish feasibility of HE BCDI at 52 keV for scatterer sizes of approximately 300 nm. This is done by analyzing the diffraction fringe contrast from a physical sample. The BCDI measurement of the standalone gold submicroparticle served the important purpose of ensuring that, with the optics configuration finally settled upon (see Appendix A), it is indeed possible to acquire a reconstructible signal from at least a prominently faceted scatterer with a well-ordered crystal lattice.

The partial coherence effect in this paper is modeled as a loss of fringe contrast due to convolution of the otherwise coherent diffraction pattern from the gold submicroparticle, with a blurring function. The formulation of this blurring kernel as a 3D Gaussian $g(\mathbf{q}) \sim \exp(-\mathbf{q}^T C \mathbf{q} / 2)$

TABLE I. Coherence lengths in different directions as estimated using $\ell = \sqrt{\hat{\mathbf{v}}^T C \hat{\mathbf{v}}}$. The width of the blurring kernel along the reciprocal lattice vector \mathbf{Q} corresponds to the longitudinal coherence lengths [35].

$\hat{\mathbf{v}}$	Description	Coherence length (nm)		Grain size (nm)
		Standard deviation	Half-width at half-maximum	
$\hat{\mathbf{x}}$	Horizontal transverse	293	345	464
$\hat{\mathbf{y}}$	Vertical transverse	306	360	406
$\hat{\mathbf{Q}}$	Longitudinal	285	336	477
$\hat{\mathbf{z}}$	Hybrid	238	280	323

in terms of the relative reciprocal space position \mathbf{q} (where C is the covariance matrix) has the advantage of providing an approximation of the coherence length $\ell_{\hat{\mathbf{v}}}$ along any direction $\hat{\mathbf{v}}$. In particular, $\ell_{\hat{\mathbf{v}}} = \sqrt{\hat{\mathbf{v}}^T C \hat{\mathbf{v}}}$, the standard deviation of the Gaussian along $\hat{\mathbf{v}}$. The Gaussian is determined from the gold particle BCDI data and is found to be largely unchanged during the subsequent reconstruction process for the grains. Table I shows the estimated coherence lengths in multiple directions. We see specifically that the estimated transverse coherence length along the vertical direction is 360 nm (half-width at half-maximum or HWHM).

Table I also lists the HWHM spread of the coherence function in the direction of the scattering vector $\hat{\mathbf{Q}}$ to be 335 nm. The coherence function in this direction has a significant contribution from the longitudinal coherence [35], which is dictated by the known bandpass of the monochromator. This provides an opportunity to compare the longitudinal coherence length estimated from BCDI to a value independently estimated from the monochromator bandwidth at 52 keV, i.e., $\Delta E/E = |\Delta\lambda/\lambda| = 10^{-4}$ [20]. The longitudinal coherence length is estimated as $\ell_{\text{long}} \simeq \lambda^2/\Delta\lambda = 238.43$ nm for $E = 52$ keV ($\lambda = 0.24$ Å). This is comparable to the estimated value in Table I, which corresponds to the width of the blurring kernel in the $\hat{\mathbf{Q}}$ direction.

The vertical transverse coherence length determined from Table I can be compared with another method of estimation from the data acquired in this experiment. Prior to each rocking scan of the grain in Fig. 4, the vertical (Y) position of the sample is readjusted inside the beam by means of a line scan along this direction that measured the aggregate Bragg-diffracted intensity on the detector. The sample is then placed at the newly determined Y position corresponding to the peak of the line profile. This routine procedure typically adjusts for potential stage drifts in between BCDI scans. The width σ_{obs} of the observed line profile results from the combined effect of two factors: (i) the scatterer width $2.35\sigma_y$ in the Y direction and (ii) the characteristic beam width σ_{beam} . The factor of 2.35 in the scatterer width accounts for the full-width at half-maximum of the Y extent of the scatterer, expressed in terms of the standard deviation σ_y of a Gaussian. If

the observed line profile is modeled as a convolution of these two effects, then we have $\sigma_{\text{obs}}^2 = \sigma_y^2 + \sigma_{\text{beam}}^2$. In our experiment, the line profile is observed to have a standard deviation of $\sigma_{\text{obs}} = 736 \pm 21$ nm while the spatial extent of the reconstructed grain is $2.35\sigma_y = 406 \pm 47$ nm. The error bounds for σ_{obs} are determined from multiple HE BCDI scans, while those for σ_y from the estimated spatial resolution of the measurement (see Appendix E).

Having acquired σ_{beam} from the measured values of σ_y and σ_{obs} , we may now approximate the demagnification effect of the lens system in the following simple way. If there is coherent illumination of the lens by an ideal plane wave, the resultant image would be a diffraction-limited spot of size σ_{DL} , which is estimated at around 554 nm at the 1-ID beamline. This quantity represents the inherent demagnification of the lens due to its finite numerical aperture. Full coherent illumination means that the coherence length at the location of the sample is equal to the diffraction-limited spot size.

However, with a partially coherent beam the same lens gives a spot size larger than the diffraction limit, larger in fact by the same factor that relates the diffraction-limited spot size to the effective transverse coherence length σ_{coh} . This relation is accessed through the approximation for the coherent fraction, given below:

$$\begin{aligned} \frac{\sigma_{\text{beam}}^2}{\sigma_{\text{DL}}^2} &= \frac{\sigma_{\text{DL}}^2}{\sigma_{\text{coh}}^2} \\ \implies \sigma_{\text{coh}} &= \frac{\sigma_{\text{DL}}^2}{\sqrt{\sigma_{\text{obs}}^2 - \sigma_y^2}} \\ &\simeq 429 \text{ nm.} \end{aligned} \quad (1)$$

This is comparable to the estimate of 360 nm obtained from analysis of the HE BCDI fringe contrast alone (Table I).

D. Complementary strain measurements

As mentioned earlier, HEDM and BCDI in their conventional forms are well-established lattice-strain characterization techniques within their respective regimes. Unifying them into a single measurement paradigm in service of material-characterization capabilities involves

careful interpretation of the obtained strain for each measurement modality. In this section we show that HEDM and BCDI are sensitive to complementary portions of the spatially varying lattice strain. Unifying these measurement methods, therefore, affords us a complete picture of the lattice strain, one that currently eludes both techniques individually.

To see this, we consider the expression for computing the strain in our BCDI measurement: $\partial u_{hkl}/\partial x_{hkl}$. Any constant displacement of the scattering centers $\mathbf{u} \rightarrow \mathbf{u} + \mathbf{C}_0$ results in a physical phase shift (i.e., a new additive constant term to $2\pi \mathbf{u} \cdot \mathbf{Q}$) but has no effect on the computed strain component. Furthermore, in typical phase-retrieval algorithms, any phase variations that are globally *linear* (i.e., over the entire scatterer volume, of the form $\mathbf{u} \sim \mathbf{C}_1 \cdot \mathbf{x}$, where \mathbf{C}_1 is a constant linear operator) are also explicitly removed prior to phase retrieval. This is typically achieved by centering the measured 3D diffraction pattern in its numerical array (since a shift in reciprocal space manifests as a linear phase ramp in real space). These variations are, of course, different from *locally* linear phase variations that may be Taylor expanded up to no higher than first order in \mathbf{x} within a small subvolume of the scatterer. We therefore see that, by design, conventional BCDI ignores constant and globally linear phase terms and is sensitive to higher-order variations in the lattice distortions. This includes deformation variations in the vicinities of phase discontinuities originating from defects and dislocations [14]. We point out that one may theoretically access the globally linear portion of the phase in BCDI by measuring the exact scattering angle, through extraordinarily careful calibration of the detector and location of the scatterer in the beam. However, this is prohibitively time consuming at BCDI beamlines presently.

On the other hand, FF HEDM is designed to be sensitive to the strain component that is homogeneous (constant) over the volume of the scatterer and which corresponds precisely to the globally linear phase ramp $\mathbf{u} \sim \mathbf{C}_1 \cdot \mathbf{x}$ that is explicitly ignored in a BCDI measurement. This quantity is alternately computed for a Bragg reflection \mathbf{Q} as $\Delta d/d = -(1/2) \cot \theta_B \Delta \theta_s$, where Δd is the change in the lattice spacing d corresponding to \mathbf{Q} , θ_B is the Bragg angle, and θ_s is the scattering angle. $\Delta \theta_s$ is the departure of the observed peak from its Debye-Scherrer ring on the detector. Appendix D of the appendix contains a perturbative analysis of the additive components of the lattice strain and their associated measurement modalities.

We, therefore, see that HEDM and BCDI are by design sensitive to different, nonoverlapping contributions to the lattice strain component. HEDM is sensitive to the spatially constant, volume-averaged component (or equivalently, the linear variations in the distortions) and not to the higher-order spatial variations. In contrast, BCDI effectively encodes the higher-order strain variations, to the deliberate exclusion of the spatially constant term

during phase retrieval. It is through a combination of both measurement modalities that the complete picture of the spatially resolved lattice strain emerges. The true value unifying the HEDM and BCDI modalities lies in obtaining this complete strain picture for polycrystalline materials, which is more than either technique is capable of providing individually.

VI. CONCLUSIONS

We demonstrate key steps towards the realization of a fully integrated multimodal high-energy diffraction-microscopy capability at synchrotron light sources. Such a capability enables enhanced *in situ* structural-imaging measurements of polycrystalline materials over four decades of length scale, in deeply embedded environments, and with strain sensitivity as fine as 1×10^{-5} . High-throughput implementation of such an approach, while impractical today due to the very limited coherence of high-energy x rays at today's third-generation light sources, is achievable at fourth-generation synchrotrons coming online in the near future that promise an up to 3 orders of magnitude increase in coherent flux within a wide range of x-ray energies. In this context, HE BCDI measurements accelerated to time scales of a few minutes integrated with HEDM will be one of the many possible means by which to capitalize on the much-improved coherence properties of these fourth-generation sources.

In particular, the multiscale method we describe could, in theory, be used to capture all relevant Bragg peaks (and, therefore, eventually spatially resolve the full strain tensor) of each grain in a polycrystalline sample, provided (i) the rotating sample itself is smaller than the beam and (ii) the grains are no larger than the coherence length (about 360 nm, from Table I). A more generalized characterization would be enabled in future high-energy, high-coherence beamlines with greater coherence volumes and the addition of the NF HEDM, which is capable of spatially resolving the crystallographic orientations of the grains in polycrystalline samples.

We note that the HE BCDI measurements envisioned in such future experiments could differ from the approach presented in this paper, which consists of a standard-practice variety of BCDI (i.e., diffraction-pattern oversampling ensured via long sample-to-detector distance, followed by reconstruction with standard algorithms). Adoption of this approach at even higher x-ray energies in the future requires special methods to address the issue of increasingly compressed reciprocal space, short of physically increasing the sample-detector distance. Recent work has been devoted to developing HE BCDI strategies by employing custom hardware [36,37], phase retrieval [38], and signal-processing solutions [39] that significantly aids in the eventual realization of coherence-aided multimodal high-energy material-microscopy methods.

A. Future challenges

We further note that the coherent volume fraction (CVF) at 52 keV in fourth-generation light sources will be significantly greater than what it is today at third-generation facilities for similar energies (comparable to the CVF at 10 keV today). While still less than the expected 10-keV CVF at fourth-generation light sources, the advantage gained by the combined HE BCDI capabilities of deeper bulk penetration and enhanced strain resolution would still present a variety of opportunities in materials characterization that have not been possible so far.

As mentioned earlier, the film grain featured in our results is chosen based on its clean diffraction signal without stray scattering from other illuminated grains, a convenience that cannot always be ensured in such a measurement. A full multiscale characterization of a given sample may well be complicated by overlapping, incoherent contributions on the area detector from multiple grains (particularly with a line-focused beam such as in our demonstrations). Such problems may be at least partially addressed in future measurements by two-dimensional constraining of the beam (either with focusing optics or suitable apertures) in order to illuminate grains more selectively. If overlapping peaks still persist, HEDM in theory provides the means to locate other Bragg reflections of the same grain elsewhere in reciprocal space, improving the chances that one or more clean Bragg peaks from a grain of interest can be identified and measured.

Coherent diffraction measurements of this kind may just as well be adopted at intermediate x-ray energies from 10 to 50 keV, as has been demonstrated at 33.6 keV in the context of ptychography [40]. However, the multiscale measurement modality described in this paper is predicated upon the proper functioning of the HEDM component of the measurement (specifically, good crystal orientation resolution and grain mapping through the capture of multiple orders of Bragg reflections). The successful capture of higher-order reflections from polycrystalline samples requires the beam energy to be 50 keV or higher, thus motivating the pursuit of BCDI at these energies. The data presented in this paper are available from [41].

ACKNOWLEDGMENTS

Conceptualization of the high-energy BCDI experiment and its integration with the far-field HEDM experimental modality, experimental demonstration of the method as well as subsequent phase retrieval and data analysis is supported by the U.S. Department of Energy, Office of Science, Basic Energy Sciences, Materials Science and Engineering Division. This research uses the resources of the Advanced Photon Source, a U.S. Department of Energy (DOE) Office of Science User Facility operated for the

DOE Office of Science by Argonne National Laboratory under Contract No. DE-AC02-06CH11357.

The paper is written by S.M. and S.O.H. The measurements are carried out by S.M., S.O.H., J.S.P., H.S., and P.K. S.S. developed the high-energy x-ray optics and optimized it for coherent diffraction measurements. The gold film is fabricated by M.J.H. The gold submicroparticle sample is provided by R.H. The phase-retrieval reconstructions and subsequent strain analysis are done by S.M. with help from S.O.H., R.H., Y.N., J.S.P., and P.K.. All authors contributed to the refining of the paper.

DATA AND CODE AVAILABILITY

The diffraction data (HEDM and BCDI) and metadata files, as well as the analysis code (PYTHON, MATLAB, and Jupyter notebooks) are available online [41]. Please contact the corresponding author for any additional questions.

APPENDIX A: CONFIGURATION OF BEAMLINE OPTICS

The FF HEDM and HE BCDI measurements are made at Beamline 1-ID-E of the Advanced Photon Source. We refer to the simplified beamline schematic in Fig. 1(a) of the main paper. Determining the optimal configuration for the optics for the HE BCDI measurements involved trying various combinations of the high-resolution monochromator (HRM), the collimating CRL, and the two vertical focusing sawtooth lenses in the x-ray beam. The configurations are tested by a visual estimate of the sharpness of the partially coherent diffraction pattern around a suitable isolated Bragg reflection from the polycrystalline gold thin film. The spot of interest is observed on a photon-counting detector at a sample-detector distance of 6.12 m and a beam energy of 52 keV (the latter is arrived at based on the constraints imposed by the HRM apparatus). The various combinations are summarized in Table II and the observed diffraction spot corresponding to four of these configurations are shown in Fig. 6. As we can see, the combination of the HRM, collimator, and the top sawtooth lens gives the best combination of fringe visibility and sharpness of the central Bragg peak. We note that since the sawtooth

TABLE II. Various configurations of beamline optics.

Configuration	Component in x-ray beam			
	HRM	Collimator	Top focusing	Bottom focusing
1	No	No	No	No
2	Yes	No	No	No
3	Yes	Yes	Yes	Yes
4	Yes	Yes	No	No
5	Yes	Yes	Yes	No
6	Yes	Yes	No	Yes

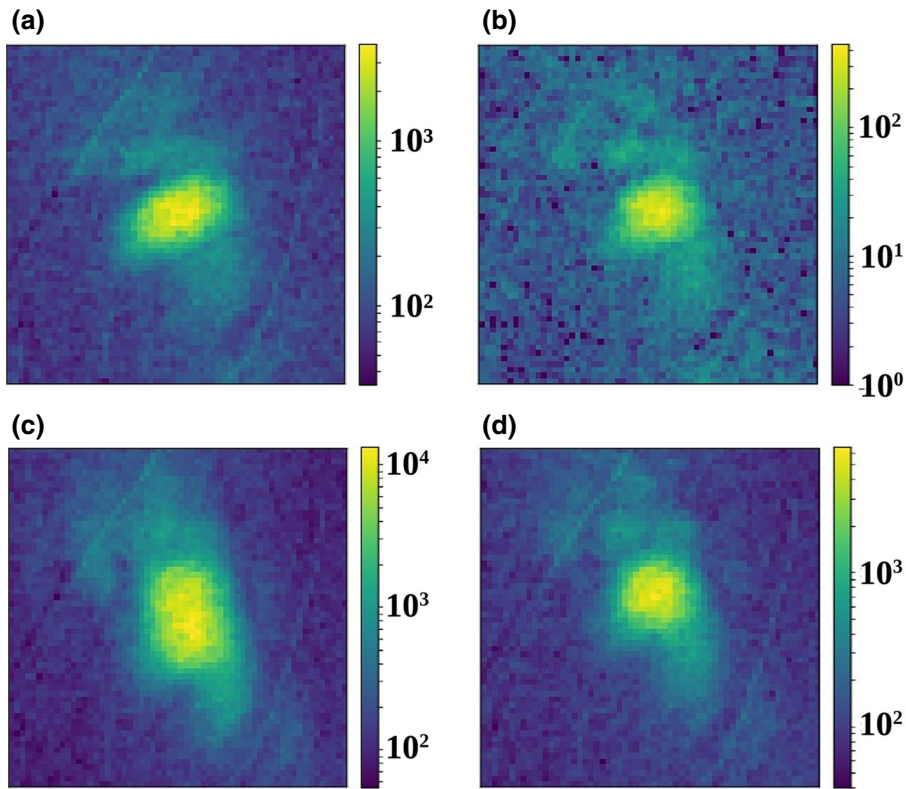


FIG. 6. The four diffraction spots, taken in order, correspond to configurations 1, 2, 3 and 5 from Table II respectively.

lenses are the farthest downstream from the x-ray source, these determined the extent of transverse coherence in the vertical direction (i.e., along the \hat{y} axis in the laboratory frame). This is the configuration used in the HE BCDI measurements throughout this paper.

APPENDIX B: PARTIALLY COHERENT DIFFRACTION IMAGING

The effect of partially coherent x-ray illumination on an isolated crystallite is modeled as a convolution of the ideal coherent diffraction pattern with a blurring function that reduces the visibility of the interference fringes [24–26]. For transmission CDI measurements at present-day synchrotron sources, this blurring kernel is very effectively modeled as a multivariate Gaussian. In this spirit we choose to model the three-dimensional partial coherence function as a multivariate Gaussian. If we consider the integer vector $N \equiv [i \ j \ k]^T$ to index the pixelated array space of the three-dimensional diffraction signal, then the blurring kernel expressed in this space is given by

$$g(N; C) = \frac{\sqrt{\det C}}{(2\pi)^{3/2}} \exp\left[-\frac{1}{2}N^T C N\right]. \quad (\text{B1})$$

Here C is a 3×3 covariance matrix that we parameterize by its eigendecomposition:

$$C \equiv R(\psi, \hat{\mathbf{n}}) \cdot D \cdot R^{-1}(\psi, \hat{\mathbf{n}}), \quad (\text{B2})$$

where D is a (necessarily) non-negative diagonal matrix with elements $\{\lambda_1^2, \lambda_2^2, \lambda_3^2\}$ and $R(\psi, \hat{\mathbf{n}})$ is a rotation matrix parameterized by the angle of rotation ψ about an axis $\hat{\mathbf{n}}$. We note that $\hat{\mathbf{n}}$ in turn is parameterized by the spherical polar and azimuthal angles: $\hat{\mathbf{n}} = \hat{\mathbf{n}}(\theta, \phi)$. The partial coherence correction step in the image reconstruction process is essentially the following optimization problem over the entire set of six blurring parameters $S \equiv \{\lambda_1, \lambda_2, \lambda_3, \psi, \theta, \phi\}$:

$$S_{\text{optimal}} = \arg \min_S \sum_N I_{\text{PC}}(N) - I_{\text{meas}}(N) \log I_{\text{PC}}(N),$$

where $I_{\text{PC}}(N) = g(N; C(S)) * I_{\text{coh}}(N)$,

(B3)

where $I_{\text{meas}}(N)$ is the measured partially coherent intensity, $I_{\text{coh}}(N)$ is the intermediate coherent diffraction intensity inferred from the phase-retrieval iterations and $*$ denotes the convolution operation. The objective function in Eq. (B3) results from the maximum-likelihood function of the Poisson-distributed intensity count of pixel N [42] and the optimization problem is solved using a simple gradient descent algorithm.

The phase-retrieval recipe to recover the complex scattering object $\rho(N)$ consists of a combination of updates to an initial guess object using the error-reduction and hybrid input-output algorithms [43]. The exact sequence of iterations is as follows:

1. 3750 iterations of error reduction.
2. 150 iterations of hybrid input-output.
3. 2750 iterations of error reduction.

The object support is initialized as a rectangle within the numerical array. A shrinkwrap algorithm [43] is employed after every 50 iterations of error reduction to update this initial estimate. The shrinkwrap operation consists of convolution of the intermediate amplitude with a smearing kernel (a Gaussian whose standard deviation varies from 3 pixels to 1 pixel in uniform steps), followed by thresholded masking at 10% of the subsequent maximum. The update of the blurring kernel for partial coherence is initiated after iteration 1250 of the first round of error reduction and is repeated after every 50 iterations of error reduction thereafter, until iteration 2500 of the second round of error reduction.

We note that while more sophisticated methods of blind deconvolution have been applied to phase retrieval [26], modeling the blurring kernel as a multivariate Gaussian has the advantage of being able to easily approximate the coherence length along any desired direction. We do this by first casting $g(N; C)$ from numerical array coordinates N to 3D reciprocal-space coordinates \mathbf{q} (with dimensions of inverse length):

$$\mathbf{q} \equiv \mathbf{B}_q N \implies N = \mathbf{B}_q^{-1} \mathbf{q}. \quad (\text{B4})$$

Here \mathbf{B}_q is a 3×3 matrix whose columns denote the discrete sampling steps in reciprocal space. This ‘‘basis’’ of sampling vectors in 3D reciprocal space depends on the scattering and sample rotation geometries and is typically determined in the course of generating the real-space image of the scatterer from the 3D complex array returned by the phase-retrieval process. Thus, we make a substitution for N in Eq. (B1) to get

$$g(\mathbf{q}; C) \sim \exp \left[-\frac{1}{2} \mathbf{q}^T \underbrace{(\mathbf{B}_q^{-T} C \mathbf{B}_q^{-1})}_{\equiv C_q} \mathbf{q} \right]. \quad (\text{B5})$$

The coherence length $\ell_{\hat{\mathbf{v}}}$ about any desired direction $\hat{\mathbf{v}}$ is simply estimated by the standard deviation of the Gaussian in this direction:

$$\ell_{\hat{\mathbf{v}}} = \sqrt{\hat{\mathbf{v}}^T C_q \hat{\mathbf{v}}}. \quad (\text{B6})$$

Table I in the main paper shows coherence lengths along specific directions computed by this method. The values are given in terms of the standard deviation as well as the more conventional half-width of the Gaussian at the half-maximum value. We see from this table that the projected grain widths along these directions are greater than the estimated coherence lengths.

APPENDIX C: STRAIN COMPUTATION

A coherent diffraction imaging measurement in the Bragg geometry is sensitive to the perturbations of the atomic positions over and above the average lattice periodicity, which may account for average strain over the volume of the crystalline scatterer as a whole. If the vector displacement of this perturbation is denoted by $\mathbf{u}(\mathbf{x})$ at a point \mathbf{x} in the scatterer bulk, the elastic strain tensor is given by

$$\mathcal{E}_{ij} = \frac{1}{2} (\partial_i u_j + \partial_j u_i), \quad (\text{C1})$$

where the indices $i, j = 1, 2, 3$ and $\partial_i \equiv \partial/\partial x_i$ denotes the partial derivative with respect to the i th coordinate. The component of the elastic strain in a direction denoted by a unit vector $\hat{\mathbf{n}}$ is given by [44]

$$\begin{aligned} \mathcal{E}(\mathbf{x} | \hat{\mathbf{n}}) &= \sum_i \sum_j \hat{n}_i \mathcal{E}_{ij} \hat{n}_j \\ &= \frac{1}{2} \sum_i \sum_j \hat{n}_i (\partial_i u_j) \hat{n}_j + \hat{n}_i (\partial_j u_i) \hat{n}_j \\ &= \frac{1}{2} \left[\sum_i \hat{n}_i \partial_i \left(\sum_j u_j \hat{n}_j \right) + \sum_j \hat{n}_j \partial_j \left(\sum_i u_i \hat{n}_i \right) \right] \end{aligned} \quad (\text{C2})$$

$$\mathcal{E}(\mathbf{x} | \hat{\mathbf{n}}) = \hat{\mathbf{n}} \cdot \nabla [\mathbf{u}(\mathbf{x}) \cdot \hat{\mathbf{n}}]. \quad (\text{C3})$$

If the reciprocal lattice point corresponding to the Bragg peak associated with a particular BCDI data set is given by \mathbf{Q} , then the measured phase from the phase-retrieval process is given by $\phi(\mathbf{x}) = 2\pi \mathbf{u}(\mathbf{x}) \cdot \mathbf{Q}$ [10]. Here, \mathbf{Q} has dimensions of inverse length, i.e., the strict reciprocal of \mathbf{u} . Thus from Eq. (C3), the strain component along the reciprocal lattice vector \mathbf{Q} is directly computed from the gradient phase:

$$\mathcal{E}(\mathbf{x} | \mathbf{Q}) = \frac{\mathbf{Q}}{|\mathbf{Q}|} \cdot \nabla \left(\frac{\phi(\mathbf{x})}{2\pi |\mathbf{Q}|} \right). \quad (\text{C4})$$

Two things become evident from Eq. C3:

1. $\mathcal{E}(\mathbf{x} | \hat{\mathbf{n}}) = \mathcal{E}(\mathbf{x} | -\hat{\mathbf{n}})$, i.e., the computed strain is the same when the phase is measured along opposing reciprocal space directions (Friedel pairs).

2. Finer resolution of the strain component is possible when computed from higher-order diffraction (i.e., larger $|\mathbf{Q}|$). This is seen by propagating the error in the measured phase into the strain: $\delta\epsilon \sim \nabla[\delta\phi]/|\mathbf{Q}|$. Herein lies another significant advantage of performing BCDI at high beam energies: higher-order Bragg peaks become accessible due to their smaller scattering angles, which is not

possible at lower x-ray energies. HE BCDI therefore has the potential to deliver strain measurements at much higher resolution than low-energy BCDI.

APPENDIX D: STRAIN ANALYSIS AND MEASUREMENT MODALITIES

The strain component along the Bragg reflection of interest is computed from the complex phase using Eq. (C4) from Appendix C above. In this equation, the locally varying phase ϕ is related to the perturbation in the atomic position \mathbf{u} by $\phi(\mathbf{x}) = 2\pi \mathbf{u}(\mathbf{x}) \cdot \mathbf{Q}$. In this section we analyze the lattice distortion and, therefore, strain perturbatively in order to ascertain exactly which components lend themselves more easily to measurement with HEDM and BCDI, and why. This distinction is important in order to understand the limitations of each measurement modality and eventually provide a comprehensive picture of the lattice strain from the multiscale measurement that we describe in this paper.

As already mentioned in the main text, the strain computed from BCDI is not sensitive to a uniform, constant vector displacement \mathbf{C}_0 of every scattering center of the crystal, i.e., a translation of the entire crystal itself. This follows from the simple fact that $\nabla[\mathbf{u}(\mathbf{x}) + \mathbf{C}_0] = \nabla\mathbf{u}(\mathbf{x})$.

Further, there may be linear ramps in the phase, originating either from a spatial offset in the diffraction pattern relative to the absolute origin of reciprocal space, or from a genuine linear lattice distortion of the form $\mathbf{u}(\mathbf{x}) = \mathbf{C}_1 \mathbf{x}$, where \mathbf{C}_1 is a constant linear operator. As is usual practice with Fourier transform-based inversion algorithms, the origin of reciprocal space is temporarily assumed to be the center of the 3D numerical array, upon which the Bragg diffraction pattern is centered prior to phase retrieval. In this process, any linear phase ramp in the subsequent real-space object is lost permanently and not recovered. From this we see that BCDI is not sensitive to the volume-averaged strain, but the fluctuations in the strain associated with lattice distortions that are over and above the linear distortions. If the phase is to be Taylor expanded about a suitable origin, then we can see that BCDI phase retrieval, by design, is sensitive only to nonlinear spatial variations in lattice distortions:

$$\phi(\mathbf{x}) = \underbrace{\phi_0 + \phi_1 \cdot \mathbf{x}}_{\text{lost information}} + \underbrace{\mathcal{O}(\mathbf{x}^2)}_{\text{seen by phase retrieval}}. \quad (\text{D1})$$

Further insight into this dependence on linear phase ramps may be obtained by differentiating Eq. (D1) to obtain the

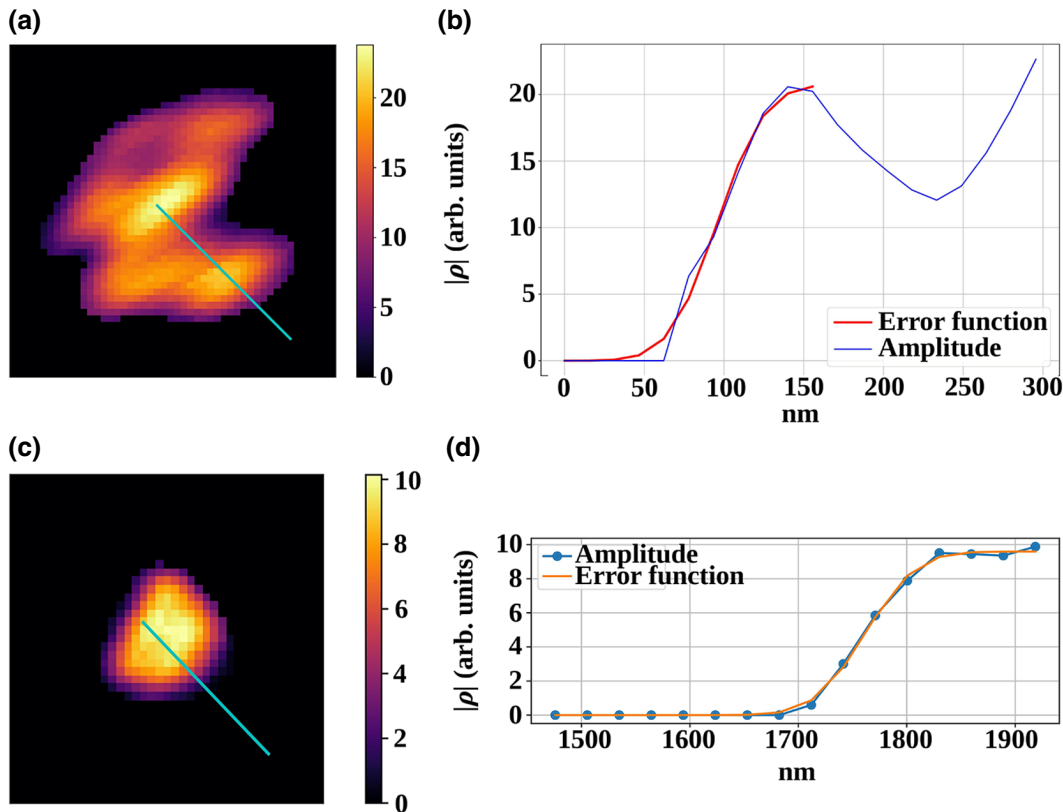


FIG. 7. (a) The amplitude $|\rho|$ of the polycrystal grain as determined from phase retrieval. (b) Variation of $|\rho|$ along the line in (a) (from the exterior to the interior of the grain), along with the error function fit to the rising edge. (c),(d) The corresponding plots for a cross section of the gold submicroparticle, with an estimated spatial resolution of 52 nm.

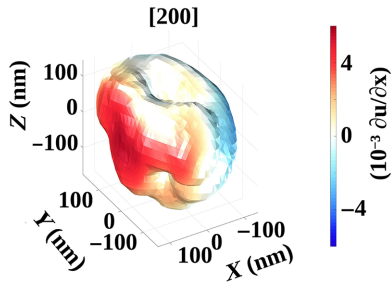


FIG. 8. Spatially resolved strain component along the surface of the smaller of the two chosen grains.

strain component:

$$\mathcal{E}(\mathbf{x}|\hat{\mathbf{n}}) \sim \underbrace{\epsilon_1}_{\text{volume-averaged strain}} + \underbrace{\mathcal{O}(\mathbf{x})}_{\text{seen by phase retrieval}}. \quad (\text{D2})$$

In particular, BCDI phase retrieval is not sensitive to the volume-averaged strain in a crystalline scatterer, but only the spatially varying strain superposed upon it. The former is analogous to the constant, “dc” component of a signal and the latter, the time-varying “ac” component whose average is zero.

APPENDIX E: ESTIMATE OF HE BCDI SPATIAL RESOLUTION

An estimate of the spatial resolution of one of the grain reconstructions is made by fitting an error function to the line profile of the amplitude of the reconstructed grain (see Fig. 7). The error function width is determined to be 47 nm, which is an estimate of the spatial resolution of the measurement.

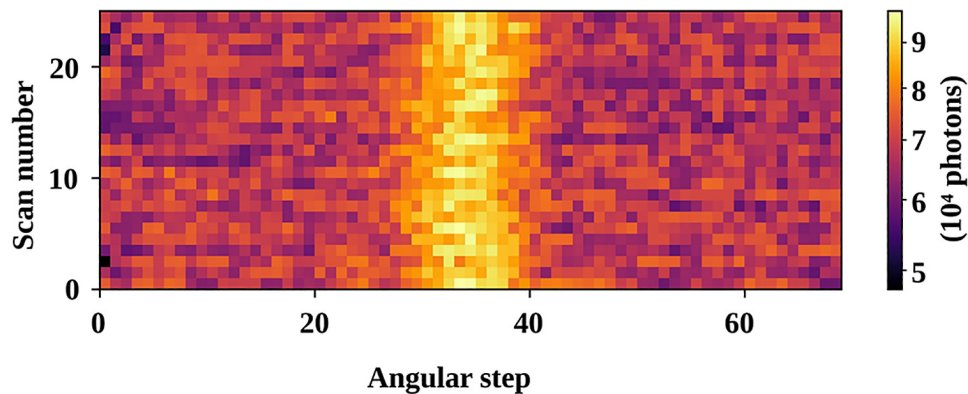


FIG. 9. Variation of the detector integrated intensity, as a function of scatterer position along the rocking direction. For each successive scan over the same angular interval, we see that the position of the Bragg reflection (indicated by the central, bright peak of the rocking curve) remains at the same angular position (approximately the 35th angular step). This indicates that there is no appreciable rotation of the isolated submicroparticle on its substrate for the duration of the measurement.

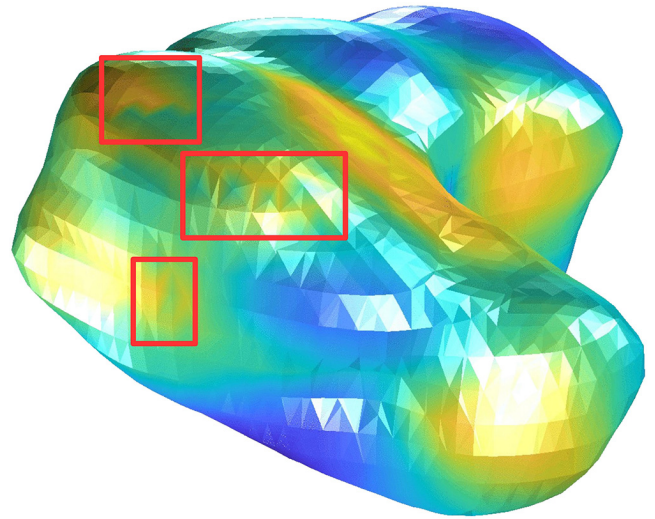


FIG. 10. Isosurface of the reconstructed raw phase of the thin-film grain (from the [111] reflection). The pixelation artifacts are highlighted.

APPENDIX F: HE BCDI FROM A (200) BRAGG PEAK

Figure 8 shows the HE BCDI reconstruction of another, smaller grain in the polycrystalline film. The partially coherent diffraction data is obtained at a very manageable scattering angle of 6.7° .

APPENDIX G: MISCELLANEOUS FIGURES

Figure 9 shows the rotational stability of the Au submicroparticle during the 10-h measurements consisting of 25 scans.

Figure 10 shows an isosurface plot of the raw, pixelated phase obtained from the reconstruction. In this image, the

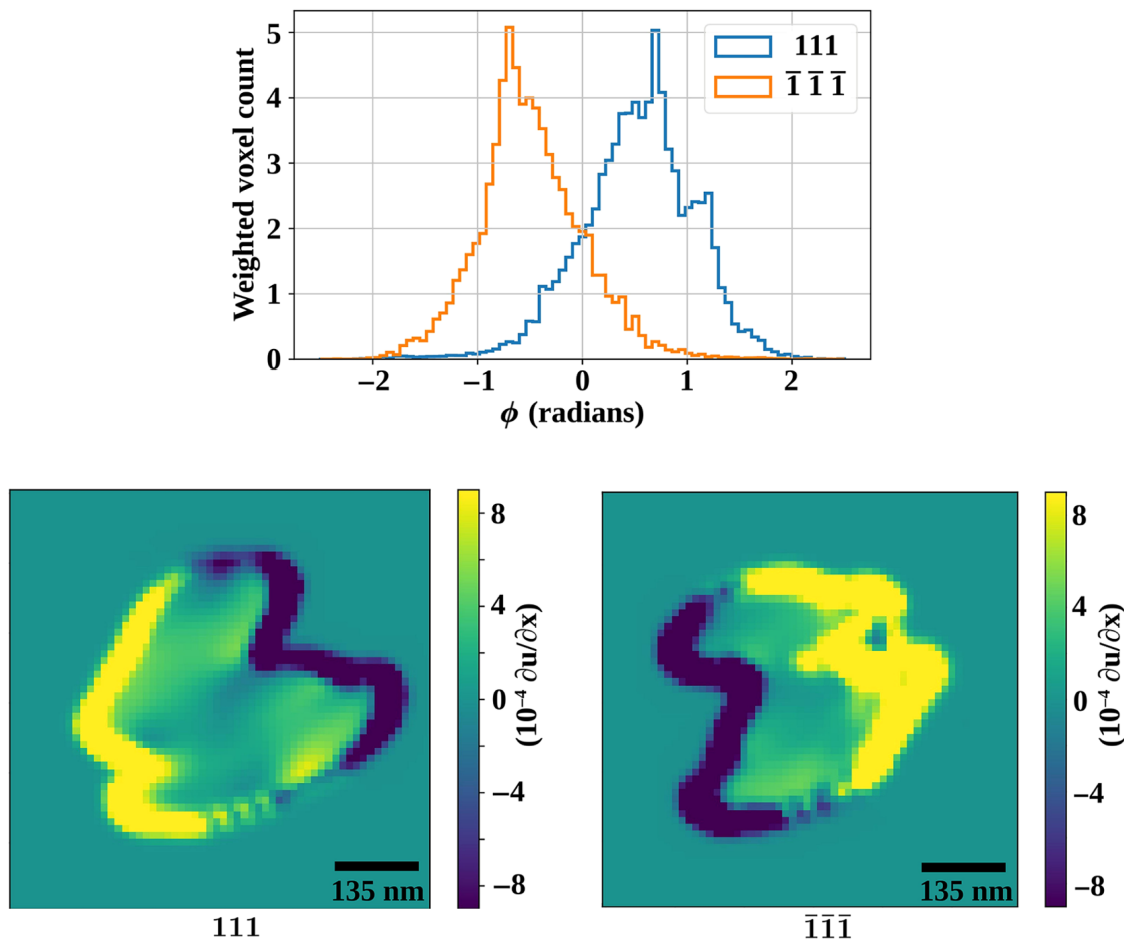


FIG. 11. (Top) Histograms of the internal phases of the Friedel-pair reconstructions. The phases are weighted with weights proportional to the reconstructed object amplitude at each pixel, and the units of the Y axis are arbitrary. The two plots indicate that the phases recovered from phase retrieval are indeed negatives of each other. (Bottom left) The central strain profile cross section of the grain in Fig. 4(g) from the main manuscript (i.e., reconstructed from the $[111]$ reflection), with the color range rescaled to highlight the strain values of the internal voxels. (Bottom right) The corresponding rescaled cross-section image for Fig. 4(j) in the main paper (from the $[\bar{1}\bar{1}\bar{1}]$ reflection).

artifacts due to the discretization without prior smoothing are clearly visible. These artifacts, when differentiated, result in significant errors in the local strain estimate.

Figure 11 shows the strain profile of the two grain reconstructions, with a rescaled color bar. While the high-strain values are along the grain boundaries, the internal strain profiles are seen to be in agreement.

[1] Andrew Ulvestad, Andrej Singer, Jesse Clark, Josh Cho, Jong Woo Kim, Ross Harder, Jorg Maser, Shirley

Meng, and Oleg Shpyrko, Topological defect dynamics in operando battery nanoparticles, *Science* **348**, 1344 (2015).
 [2] A. Ulvestad, M. J. Welland, S. S. E. Collins, R. Harder, E. Maxey, J. Wingert, A. Singer, S. Hy, P. Mulvaney, P. Zapol, and O. G. Shpyrko, Avalanching strain dynamics during the hydriding phase transformation in individual palladium nanoparticles, *Nat. Commun.* **6**, 10092 (2015).
 [3] S. O. Hruszkewycz, M. V. Holt, C. E. Murray, J. Bruley, J. Holt, A. Tripathi, O. G. Shpyrko, I. McNulty, M. J. Highland, and P. H. Fuoss, Quantitative nanoscale imaging of lattice distortions in epitaxial semiconductor heterostructures using nanofocused x-ray bragg projection ptychography, *Nano Lett.* **12**, 5148 (2012).

- [4] M. J. Highland, S. O. Hruszkewycz, D. D. Fong, Carol Thompson, P. H. Fuoss, I. Calvo-Almazan, S. Maddali, A. Ulvestad, E. Nazaretski, X. Huang, H. Yan, Y. S. Chu, H. Zhou, P. M. Baldo, and J. A. Eastman, In-situ synchrotron x-ray studies of the microstructure and stability of in2o3 epitaxial films, *Appl. Phys. Lett.* **111**, 161602 (2017).
- [5] S. O. Hruszkewycz, S. Maddali, C. P. Anderson, W. Cha, K. C. Miao, M. J. Highland, A. Ulvestad, D. D. Awschalom, and F. J. Heremans, Strain annealing of sic nanoparticles revealed through bragg coherent diffraction imaging for quantum technologies, *Phys. Rev. Mater.* **2**, 086001 (2018).
- [6] R. M. Suter, C. M. Hefferan, S. F. Li, D. Hennessy, C. Xiao, U. Lienert, and B. Tieman, Probing microstructure dynamics with x-ray diffraction microscopy, *J. Eng. Mater. Technol.* **130**, 021007 (2008).
- [7] Jay C. Schuren, Paul A. Shade, Joel V. Bernier, Shiu Fai Li, Basil Blank, Jonathan Lind, Peter Kenesei, Ulrich Lienert, Robert M. Suter, Todd J. Turner, Dennis M. Dimiduk, and Jonathan Almer, New opportunities for quantitative tracking of polycrystal responses in three dimensions, *Curr. Opin. Solid State Mater. Sci.* **19**, 235 (2015), *Opportunities in Mesoscale Science*.
- [8] I. K. Robinson, I. A. Vartanyants, G. J. Williams, M. A. Pfeifer, and J. A. Pitney, Reconstruction of the Shapes of Gold Nanocrystals Using Coherent X-ray Diffraction, *Phys. Rev. Lett.* **87**, 195505 (2001).
- [9] Jianwei Miao, Tetsuya Ishikawa, Ian K. Robinson, and Margaret M. Murnane, Beyond crystallography: Diffractive imaging using coherent x-ray light sources, *Science* **348**, 530 (2015).
- [10] Ian Robinson and Ross Harder, Coherent x-ray diffraction imaging of strain at the nanoscale, *Nat. Mater.* **8**, 291 (2009).
- [11] S. O. Hruszkewycz, M. Allain, M. V. Holt, C. E. Murray, J. R. Holt, P. H. Fuoss, and V. Chamard, High-resolution three-dimensional structural microscopy by single-angle bragg ptychography, *Nat. Mater.* **16**, 244 (2017).
- [12] Allison Yau, Wonsuk Cha, Matthew W. Kanan, G. Brian Stephenson, and Andrew Ulvestad, Bragg coherent diffractive imaging of single-grain defect dynamics in polycrystalline films, *Science* **356**, 739 (2017).
- [13] N. Vaxelaire, S. Labat, T. W. Cornelius, C. Kirchlechner, J. Keckes, T. Schulli, and O. Thomas, New insights into single-grain mechanical behavior from temperature-dependent 3-d coherent x-ray diffraction, *Acta Mater.* **78**, 46 (2014).
- [14] Mathew J. Cherukara, Reeju Pokharel, Timothy S. O'Leary, J. Kevin Baldwin, Evan Maxey, Wonsuk Cha, Jorg Maser, Ross J. Harder, Saryu J. Fensin, and Richard L. Sandberg, Three-dimensional x-ray diffraction imaging of dislocations in polycrystalline metals under tensile loading, *Nat. Commun.* **9**, 3776 (2018).
- [15] R. M. Suter, D. Hennessy, C. Xiao, and U. Lienert, Forward modeling method for microstructure reconstruction using x-ray diffraction microscopy: Single-crystal verification, *Rev. Sci. Instrum.* **77**, 123905 (2006).
- [16] J. V. Bernier, N. R. Barton, U. Lienert, and M. P. Miller, Far-field high-energy diffraction microscopy: A tool for intergranular orientation and strain analysis, *J. Strain Anal. Eng. Des.* **46**, 527 (2011).
- [17] Kartik Kapoor and Michael D. Sangid, Initializing type-2 residual stresses in crystal plasticity finite element simulations utilizing high-energy diffraction microscopy data, *Mater. Sci. Eng.: A* **729**, 53 (2018).
- [18] John L. Barber, Cris W. Barnes, Richard L. Sandberg, and Richard L. Sheffield, Diffractive imaging at large fresnel number: Challenge of dynamic mesoscale imaging with hard x rays, *Phys. Rev. B* **89**, 184105 (2014).
- [19] Y. Ivanyushenkov, K. Harkay, M. Borland, R. Dejus, J. Dooling, C. Doose, L. Emery, J. Fuerst, J. Gagliano, Q. Hasse, *et al.*, Development and operating experience of a 1.1-m-long superconducting undulator at the advanced photon source, *Phys. Rev. Accelerators Beams* **20**, 100701 (2017).
- [20] S. D. Shastri, Combining flat crystals, bent crystals and compound refractive lenses for high-energy x-ray optics, *J. Synchrotron Radiat.* **11**, 150 (2004).
- [21] S. D. Shastri, J. Almer, Carolina Ribbing, and Björn Cederrström, High-energy x-ray optics with silicon saw-tooth refractive lenses, *J. Synchrotron Radiat.* **14**, 204 (2007).
- [22] Erika Benda, Jonathan Almer, Peter Kenesei, Ali Mashayekhi, John Okasinski, Jun-Sang Park, Rogelio Ranay, and Sarviyt Shastri, *Minimizing Experimental Setup Time and Effort at Aps Beamline 1-ID Through Instrumentation Design*, Type Tech. Rep. (Argonne National Lab.(ANL), Argonne, IL, United States, 2016).
- [23] Jianwei Miao, Pambos Charalambous, Janos Kirz, and David Sayre, Extending the methodology of x-ray crystallography to allow imaging of micrometre-sized non-crystalline specimens, *Nature* **400**, 342 (1999).
- [24] Chanh Quoc Tran, Andrew Gareth Peele, A. Roberts, Keith A. Nugent, D. Paterson, and I. McNulty, Synchrotron beam coherence: A spatially resolved measurement, *Opt. Lett.* **30**, 204 (2005).
- [25] Jesse N. Clark and Andrew G. Peele, Simultaneous sample and spatial coherence characterisation using diffractive imaging, *Appl. Phys. Lett.* **99**, 154103 (2011).
- [26] J. N. Clark, X. Huang, R. Harder, and I. K. Robinson, High-resolution three-dimensional partially coherent diffraction imaging, *Nat. Commun.* **3**, 993 (2012).
- [27] J. R. Fienup, Phase retrieval algorithms: A comparison, *Appl. Opt.* **21**, 2758 (1982).
- [28] S. Marchesini, H. He, H. N. Chapman, S. P. Hau-Riege, A. Noy, M. R. Howells, U. Weierstall, and J. C. H. Spence, X-ray image reconstruction from a diffraction pattern alone, *Phys. Rev. B* **68**, 140101 (2003).
- [29] W. Cha, A. Ulvestad, M. Allain, V. Chamard, R. Harder, S. J. Leake, J. Maser, P. H. Fuoss, and S. O. Hruszkewycz, Three Dimensional Variable-Wavelength X-ray Bragg Coherent Diffraction Imaging, *Phys. Rev. Lett.* **117**, 225501 (2016).
- [30] Hemant Sharma, Richard M. Huizenga, and S. Erik Offerman, A fast methodology to determine the characteristics of thousands of grains using three-dimensional x-ray diffraction. II. Volume, Centre-of-mass position, crystallographic orientation and strain state of grains, *J. Appl. Crystallogr.* **45**, 705 (2012).
- [31] Hemant Sharma, Richard M. Huizenga, and S. Erik Offerman, A fast methodology to determine the characteristics of thousands of grains using three-dimensional x-ray

- diffraction. I. Overlapping diffraction peaks and parameters of the experimental setup, *J. Appl. Crystallogr.* **45**, 693 (2012).
- [32] Wolfgang Ludwig, Søren Schmidt, Erik Mejdal Lauridsen, and Henning Friis Poulsen, X-ray diffraction contrast tomography: A novel technique for three-dimensional grain mapping of polycrystals. I. Direct beam case, *J. Appl. Crystallogr.* **41**, 302 (2008).
- [33] Marcus C. Newton, Steven J. Leake, Ross Harder, and Ian K. Robinson, Three-dimensional imaging of strain in a single ZnO nanorod, *Nat. Mater.* **9**, 120 (2010).
- [34] Felix Hofmann, Edmund Tarleton, Ross J. Harder, Nicholas W. Phillips, Pui-Wai Ma, Jesse N. Clark, Ian K. Robinson, Brian Abbey, Wenjun Liu, and Christian E. Beck, 3D lattice distortions and defect structures in ion-implanted nano-crystals, *Sci. Rep.* **7**, 45993 (2017).
- [35] Steven J. Leake, Marcus C. Newton, Ross Harder, and Ian K. Robinson, Longitudinal coherence function in x-ray imaging of crystals, *Opt. Express* **17**, 15853 (2009).
- [36] Anders Filsø Pedersen, Virginie Chamard, and Henning Friis Poulsen, Numerical study of bragg cdi on thick polycrystalline specimens, *Opt. Express* **26**, 23411 (2018).
- [37] A. F. Pedersen, V. Chamard, C. Detlefs, T. Zhou, D. Carbone, and H. F. Poulsen, X-ray coherent diffraction imaging with an objective lens: Towards three-dimensional mapping of thick polycrystals, *Phys. Rev. Res.* **2**, 033031 (2020).
- [38] S. Maddali, M. Allain, W. Cha, R. Harder, J.-S. Park, P. Kenesei, J. Almer, Y. Nashed, and S. O. Hruszkewycz, Phase retrieval for Bragg coherent diffraction imaging at high x-ray energies, *Phys. Rev. A* **99**, 053838 (2019).
- [39] S. Maddali, I. Calvo-Almazan, J. Almer, P. Kenesei, J.-S. Park, R. Harder, Y. Nashed, and S. O. Hruszkewycz, Sparse recovery of undersampled intensity patterns for coherent diffraction imaging at high x-ray energies, *Sci. Rep.* **8**, 4959 (2018).
- [40] Julio Cesar Da Silva, Alexandra Pacureanu, Yang Yang, Sylvain Bohic, Christian Morawe, Raymond Barrett, and Peter Cloetens, Efficient concentration of high-energy x-rays for diffraction-limited imaging resolution, *Optica* **4**, 492 (2017).
- [41] S. Maddali, J.-S. Park, H. Sharma, S. Shastri, P. Kenesei, J. Almer, R. Harder, M. J. Highland, Y. Nashed, and S. O. Hruszkewycz, Data for: High-Energy Coherent X-Ray Diffraction Microscopy of Polycrystal Grains: Steps Toward a Multiscale Approach, <https://bit.ly/2DgtQ0E> (2020).
- [42] Pierre Godard, Marc Allain, Virginie Chamard, and John Rodenburg, Noise models for low counting rate coherent diffraction imaging, *Opt. Express* **20**, 25914 (2012).
- [43] S. Marchesini, Invited article: A unified evaluation of iterative projection algorithms for phase retrieval, *Rev. Sci. Instrum.* **78**, 011301 (2007).
- [44] Rob Phillips, *Crystals, Defects and Microstructures: Modeling Across Scales* (Cambridge University Press, Cambridge, UK, 2001).